Membrane-tethered cadherin substrates reveal actin architecture at adherens junctions

Sayantika Ghosh*[#], John James*, Badeer Hassan Ummat, Darius Köster

University of Warwick, Warwick Medical School - Division of Biomedical Sciences and Centre for Mechanochemical Cell Biology, CV4 7AL, Coventry, UK

**contributed equally*
[#]current affiliation: University of Cambridge, Department of Biochemistry, Sanger Building, 80 Tennis Court Road, Cambridge, CB2 1GA

Abstract

Adherens junctions (AJ) are E-cadherin-based adhesions at cell-cell contacts that connect the actin cytoskeleton of epithelial cells. The formation and maturation of these junctions is important in development, e.g. for the generation of epithelial tissues, and loss of adherens junctions is linked to metastasis in cancer. It is well established that AJ is a mechano-sensitive process involving the clustering of E-cadherins within the plasma membrane of cells and across adjacent cells, and the mechanical activation of α-catenins that connect E-cadherins with the actin cytoskeleton. However, how membrane mobility of E-cadherins and their organisation in time and space influence this process is less well understood, partly due to limitations to control the physical properties of cell membranes and perform high resolution in model organisms or cell monolayers. Here we place MCF7 cells labelled with fluorescent actin, e-cadherin, and α-catenin, on fluid-supported lipid bilayers containing the extracellular domain of cadherin as a biomimetic system to enable super resolution TIRF-SIM imaging of AJ. We found that MCF7 cells were able to attach and spread on these substrates, recruiting E-cadherin and α-catenin to form AJs that can mature and are mobile. Interestingly, we found that, depending on the mobility of E-cadherin within the SLB, distinct types of actin architecture emerge over time. Low mobility substrates support formin-based linear polymerisation while high mobility substrates support Arp2/3 -based branched actin polymerisation. These regions are spatially delimited within the cell and can change over time, giving rise to a mature state containing regions of both branched and linear actin.

Introduction

Cells in epithelial tissues are held together by adherens junctions (AJs) formed by E-cadherin interactions at the apical pole of the cell. These structures serve as mechanical anchors and contact points for biochemical and mechanical signalling. Mechano-signalling from AJs is essential to regulate in cells processes like migration and proliferation, and the mechanical forces generated and sensed by these structures depend on the architecture of the underlying actin cytoskeleton.

AJs are formed when the extracellular domain of E-cadherin of adjacent cells interact with each other. Intracellular domains of E-cadherin can recruit and form a complex with β-catenin and the α-catenin head domain. The tail domain of α-catenin can then bind to actin, forming a link between the actin cytoskeleton of adjacent cells. Actin in conjunction with myosin can exert a pulling force on the adhesion, unfurling α-catenin to reveal cryptic binding sites for vinculin. Vinculin not only reinforces the AJs by simultaneously binding α-catenin and actin, but also contributes to bundling of actin, potentially by dimerisation of its tail domain. This intracellular recruitment of AJ proteins is accompanied by a clustering of E-cadherin, by both homotypic (cis-clustering of E-cadherins on the same plasma membrane) and heterotypic interactions (trans-clustering of E-cadherins on the membrane of adjacent cells) of their extracellular domains, thus forming mature AJs. A combination of cadherins internalised as vesicles and flowing in from the surrounding membrane constantly replenishes and maintains these AJs (1, 2)

The actin cytoskeleton undergoes remodelling during the maturation of a cell-cell contact. When two cells come into contact, actin polymerisation at the junction keeps the membranes together. Linear actin polymerisation factors such as Formin1 (3), mDia1 (4) and FMNL2 (5) have been reported to be present in AJs as well as mENA/Vasp proteins. The branched actin network polymerising protein Arp2/3 along with its activators WAVE and IQGAP2 is also recruited into AJs (6). The combination of actin branch generation by Arp2/3 along filaments extended by formins can give rise to exponentially expanding actin networks that can create pushing forces at the membrane. Indeed, Arp2/3 recruitment at AJs has been consistently correlated with increased junction stability. As a junction matures, the actin unbranching protein Coronin1B is recruited, and remodels branched actin networks into bundles of linear actin filaments (7).

The classical view of a mature cell-cell contact has these linear bundles stretched taut between AJs parallel to the cell surface. Cell plasma membranes are held together by extracellular E-cadherin interactions and tension across these bundles. However, recent evidence has shown that different types of actin architecture can exist, and together with the actin cytoskeleton, the distribution of AJs along a cell-cell contact evolves over time. Studies in cell monolayers have reported linear bundles of actin filaments perpendicular to the surface of cell-cell contacts and attached to AJ puncta distributed radially around the cell. Branched actin protrusions have been discovered to continue to push against cell membranes at mature cell-cell contacts, potentially as a mechanism for repair (8).

Because AJs form between cells at the apical pole of an epithelial monolayer, with high and super-resolution, live cell imaging capturing the dynamics of the molecular components of AJs has proved difficult, particularly when it comes to resolving dynamics along the cell-cell contact plane. To overcome these drawbacks, several studies have imaged cells adhering to E-cadherins immobilised on coverslips directly, but these systems offer limited insights into AJ formation as important aspects such as lateral mobility of E-cadherin and its clustering cannot be fully recapitulated (9). Alternatively, E-cadherin molecules attached to supported lipid bilayers formed on glass coverslips represent a readily available system to incorporate these parameters (10, 11). This system is predestined for study of cell adhesion dynamics in live cells, and a recent study by the Heisenberg lab has revealed how actomyosin flows are coupled with the extracellular domain of E-cadherin (E-cad-ECD) during the first hour of adhesion in zebrafish ectoderm progenitor cells (12).

In the present study, we employ the powers of SLB decorated with E-cad-ECD to study the organisation of the actin network, E-cadherin, and alpha-catenin in MCF-7 cells, a cell line derived from breast cancer tissue and commonly used to study E-cadherin-based cell adhesion (13). Using total internal reflection fluorescence (TIRF) and TIRF- structural illumination microscopy (SIM), we follow protein dynamics during AJ formation and maturation up to four hours post-adhesion. We discover that at later time points (post 2 hours) E-cadherin mobility directs the formation of regions at the cell-SLB interface that are dominated by Arp2/3 and formin-driven actin polymerisation. This indicates that cells sense the mobility of the ligand to direct their actin cortex activation during AJ formation.

Results

MCF7 cells form adherens junctions on SLBs containing E-cadherin-ECD

MCF7 E-cadherin-GFP knock in cells additionally expressing LifeAct-TagRFPT and iRFP670-α-catenin (13) were seeded onto supported lipid bilayers (96% DOPC, 4% DGS-NTA(Ni^{2+})) decorated with His_6-E-cad-ECD (Fig. 1). TIRF imaging revealed that MCF7 cells are able to attach and spread on these substrates, covering on average an area of 68.7 μm^2 (Fig 1 a,b). The cell spreading area increased within the first 60 min and then plateaued, indicating that the cell spreading reached a steady state at that time. As reported earlier, cell spreading is driven by actin-rich protrusions that grow from the edge of the cell along the SLB. Although the protrusion area decreases over time, they persist once the cell has reached its maximum spreading area (Fig 1c). Together with actin, e-cadherin and α-catenin are recruited to the anterior surface of the cell, indicating that AJs are being formed at the cell-SLB interface (Fig 1 d-f). Interestingly, the recruitment of AJ

proteins continues even after the end of cell spreading, suggesting that new AJ formation and maturation can be visualised at later time points.

To this end, we used TIRF-SIM imaging to obtain super-resolution images of AJs at different stages of maturation (Fig 2a). At the edge of the protrusions, we found E-cadherin puncta at the tips of the actin bundles, presumably where they are attached to the substrate because they are clearly visible during tens of seconds using TIRF-SIM, which only excites fluorophores within the first ~100 nm above the surface of the glass coverslip. These early adhesions are characterised by the presence of E-cadherin but without detectable α-catenin (green arrows). Following these adhesions over time reveals the elongation of the E-cadherin signal (yellow arrows) indicating further clustering of E-cadherin along actin protrusions, as well as the recruitment of α-catenin (red arrows), which are hallmarks of the maturation of cadherin puncta in AJ. Within the protrusion, we see that the position of AJs changes with time (Fig 2b), suggesting that they bind to the actin cytoskeleton within the protrusions and are pulled in by retracting filaments or retrograde flow. Tracking these AJs shows that they move along actin filaments leading to further clustering (Fig 2c). Concomitantly, at the base of the protrusion, we see an enrichment of mature AJs indicated by an increase in actin, E-cadherin, and α-catenin.

Actin Architecture at the Cell-SLB Interface

During the process of cells adhering onto E-cadherin decorated SLBs, we can identify four types of actin organisation: disperse filaments, retrograde flow, static bundles, and dynamic patches (Fig 3a). Disperse filaments are scattered throughout the cell interior and are distinct from static bundles, which are thicker linear structures that do not move. Retrograde flow is found at the cell edge and in protrusions, which is in line with observations of cells plated on substrates with immobilised e-cadherin or extracellular matrix proteins. Static bundles appear in spatially delimited regions, where they appear to be aligned, and the strong actin signal indicates that they are made of multiple actin filaments. Both static bundles and dispersed filaments seem to be distinct from stress fibres previously observed in cells on immobilised e-cadherin or extracellular matrix. They do not show the minimal curvature expected for stress fibres under tension. Dynamic patches are characterised by their changing actin filament organisation on a minute timescale and by the fact that they do not show any longer linear actin structures (Fig 3a).

Upon imaging, we found that these structures photo-bleach (Fig 3a), and quantification of the rate of photobleaching revealed differences between the different actin structures (Fig 3b, c). The photo-bleaching rate is highest for disperse filaments, and about 1.7 times faster than static bundles and 2.4 times faster than retrograde flow or dynamic patches. This indicates that the rate of actin polymerisation, delivering new LifeAct-TagRFPT into the actin structures, is higher in these three types of actin structures compared to the dispersed filaments. Retrograde flow and dynamic patches photobleach less than static bundles, suggesting that they are maintained by distinct processes, the former of which gives rise to faster actin polymerisation.

Branched and linear actin polymerisation are differentially regulated

Since branched actin polymerisation is known to be prevalent at cell edges of protruding and spreading cells, and given the appearance of the organisation of the actin network observed in dynamic patches, we hypothesised that retrograde flow and dynamic patches are maintained by Arp2/3-mediated actin polymerisation. Due to the linear actin filaments observed in static bundles, we assumed that these are maintained by formin-mediated actin polymerisation. We performed time lapse imaging of cells adhering to DPPC-SLBs that display low mobility E-cad-ECD (Sup. Fig. 1), which favours the appearance of static actin bundles >2 h of cell attachment. Static actin bundles elongate at a rate of 6 (± 3) nm s-1, which was measured by generating a kymograph along the direction of extension (Fig 2 a, b). We found that the rate of elongation decreased 3 times to 2 (± 1) nm s^{-1} when cells were treated with the formin inhibitor SMIFH2 (Fig. 2c). Interestingly, we found that a 1.5 fold decrease in the elongation rate to 4 (± 2) nm s^{-1} occurred in cells plated on DOPC SLBs displaying a higher mobility of E-cad-ECD (Sup. Fig. 1). Together these results suggest that formin-mediated linear actin polymerisation is upregulated when the cell engages with E-cad-ECD tethered to more viscous lipid bilayers.

Using a similar kymograph-based approach, we analysed the rates of actin retrograde flow in protrusions of cells adhering to E-cad-ECD-tethered SLBs of high and low mobility (Fig 2 d). We found that retrograde flow increases 1.5 times when cells are seeded onto high mobility DOPC SLB (15 (± 5) nm s^{-1}) compared to low mobility DPPC SLB (10 (± 2) nm s^{-1}) (Fig. 2 e). Treatment of these cells with the Arp2/3 inhibitor CK-666 resulted in a three-fold decrease in retrograde flow (2 (± 1) nm s^{-1})(Fig 2d). This shows that Arp2/3 is a major factor in actin polymerisation at the cell edge and that retrograde flow is activated in cells adhering to E-cad-ECD on more fluid SLBs.

Turning now our attention to the dynamic actin patches, the lack of a clear directionality of actin motion, and the fact that we could not employ the kymograph analysis. Instead, we use particle image velocimetry (PIV) to map directional changes of the actin signal over time in and around dynamic actin patches (see methods). Although the spatially averaged values of actin flow obtained by PIV are typically lower than the flows obtained by kymograph analysis, we can observe a 1.2 fold difference in actin flow amplitudes between cells in high- and low-mobility SLBs: apparent actin flow in cells on low-mobility DPPC SLBs is 3.3 (± 0.2) nm s^{-1}, while it is 4.0 (± 0.2) nm s^{-1} on high-mobility DOPC SLBs (Fig. 4 g). Actin flows in dynamic patches decrease by a factor of 2 to 2 (± 0.3) nm s^{-1} in cells treated with CK666. This suggests that dynamic patches are areas of Arp2/3 activity and that they show a similar response to E-cad-ECD mobility as actin structures displaying retrograde flow indicating that both are regulated by related pathways. Taken together, these results suggest that a switch between Arp2/3-mediated branched actin polymerisation and formin-mediated linear actin polymerisation can be controlled by changes in the mobility of the E-cad-ECD with which the cell engages.

We then proceeded to look at how these branched and linear networks develop over the time of formation of the cell-cell contact. We seeded cells on high mobility DOPC SLBs containing E-cad-ECD and imaged them at different time points post seeding (Fig 5a). We quantified areas of the cell showing either type of the above defined actin architectures (Fig. 5 b). At 1 h post seeding, we see dispersed filaments at the inside of the cell-SLB interface and retrograde flow at the cell edge with large protrusions as the cell is still spreading. 2 hours after seeding, we see that most of the cell area is covered with static bundles and the protrusions are basically gone. Small areas between the static bundles display a more disperse actin network and at 4 h post-seeding, the disperse filaments take up a larger area and separate the static bundles into compartments. 5 h after seeding, these static bundles are replaced by dynamic patches of actin. Together, these results suggest that the initial stages of cell contact formation involve both branched and linear actin networks (Fig 5c). Linear networks seem to predominate in intermediate stages of maturation, after which branched networks become active again.

Discussion

We have shown that our system is apt for generating mobile AJs on surfaces ideal for TIRF-SIM imaging. We have shown that an increase in cadherin mobility favours Arp2/3 activity while a decrease in cadherin mobility favours linear actin polymerisation by formins. We analyse the temporal changes in the actin architecture and find them consistent with previous reports of actin and its polymerisers in AJs (4-6). Early cell-cell contacts are enriched in branched actin that is reorganised into linear bundles. This switch from branched to linear actin networks is also evident from the initial TIRF experiments, where we see a decrease in protrusion size consistent with a decrease in Arp2/3 activity after 1 h post-attachment. Reactivation of branched actin in later stages is also consistent with recent studies showing that Arp2/3 reappears in late cell-cell contacts, potentially as a repair mechanism (14).

The actin architecture that we see 1 h after seeding is remarkably similar to those reported in zebrafish ectoderm progenitor cells at the same time (12). This suggests that the processes we study are conserved across cell lines and species. We have additionally studied the progress of this actin architecture as the cell-cell contact evolves over time and observed the more intricate structures, which led us to a better understanding of polymerisation dynamics. The same study also reports a flow of actin along with the actin-binding proteins myosin and ezrin from the cell interior to the periphery. Consistently, we observe a

flow of actin and AJs from protrusions inward to the periphery of the cell cortex, where we see an enrichment of actin.

Using TIRF-SIM superresolution imaging of the cell-SLB interface at later time points (>2h post attachment) has revealed interesting and exciting actin network dynamics with the appearance of dynamic actin patches and regions of seemingly stable actin bundles. First, we find that both dynamic patches and areas of retrograde flow behave similarly in all measures we have studied. This suggests that they are maintained by the same processes, activation of Arp2/3, likely by the Rac1 pathway, which mediates polymerisation of branched actin networks. On the other hand, static bundles are maintained by formins that are likely activated by the RhoA pathway. The fact that dynamic patches and static bundles appear as spatially confined structures along the cell-SLB interface, that they can move laterally, and change over time suggests that RhoA and Rac1 linked pathways are confined in local zones along the cell-SLB interface (15). Interestingly, the mobility of E-cad-ECD, and with this the amount of traction force that cells generate when dragging e-cadherins along the cell surface, directs which pathway is preferred. The Heisenberg laboratory recently reported global regulation of RhoA during the first hour of cell-SLB adhesion (12); however, the appearance of local zones with distinct actin patterns reported in this study is new and opens the path to investigate the biochemical and physical mechanisms that allow the cell to sense local differences in the mobility of E-cadherin.

Materials and Methods

Preparation of Supported Lipid Bilayers and Experimental Chambers

Supported lipid bilayers and the experimental chambers were prepared as described earlier (16). Glass coverslips (25 mm diameter, #1.5 borosilicate, Gerhard Menzel GmbH, cat. no. LDRND25/1.5) for SLB formation were cleaned with 2% Hellmanex III solution (Hellma Analytics, cat. No. Z805939, Merck) following the manufacturer's instructions, thoroughly rinsed with MilliQ water, then placed in a 3M KOH (Sigma-Aldrich) solution and sonicated for 15 mins, again thoroughly rinsed with MilliQ water and finally blow dried under a stream of N_2 gas.

Experimental chambers were made by cutting off the lid and conical bottom part of 0.2 ml PCR tubes (cat. no. I1402-8100, Starlab) and sticking the remaining cylinder onto the cleaned coverslip glass using UV glue (cat. no. NOA88, Norland Products) and three minutes curing by intense UV light at 265 nm (UV Stratalinker 2400, Stratagene). Freshly cleaned and assembled chambers were directly used for experiments.

Supported lipid bilayers (SLB) containing 96% of DOPC lipids (cat. no. 850375, Avanti Polar Lipids) for high mobility membranes or DPPC lipids (cat. no. 850355P, Avanti Polar Lipids) for low mobility membranes and 4% DGS-NTA(Ni^{2+}) lipids (cat. no. 790404, Avanti Polar Lipids) were formed by fusion of small uni-lamellar vesicles (SUV) that were prepared by lipid extrusion using a membrane with 100 nm pore size (cat. no. 610000, Avanti Polar Lipids) (see for detailed procedure). SLBs were formed by addition of 10 µl of SUV mix at 4 mM lipid concentration to chambers filled with 90 µl SLB buffer (1xTBS solution, pH 7.4), incubated for 25 min and then washed 10 times with SLB buffer. Extrusion and SLB formation were performed at RT for the DOPC containing lipid mix and at T = 40-45˚C for the DPPC containing lipid mix to ensure formation of uniform lipid bilayers.

Glass slides were mounted into AttoFluor metal chambers (cat. no. A7816, Invitrogen) for imaging on inverted microscopes. For live cell imaging using TIRF-SIM, no small chambers were used and SLBs were formed on the entire glass coverslip. Cleaned glass coverslips were mounted into AttoFluor chambers and SLB were formed by adding 120ul of SUV was added to 300ul SLB formation buffer.

Cell Culture

MCF 7 E-cad-GFP CRISPR-Cas9 knock in cells transduced with LifeAct-TagRFPT and iRFP670-α-catenin were a gift from Ivar Noordstra (Alpha Yap Laboratory). Cells were cultured in Dublecco's Modified Eagle Media (DMEM) with Glutamax (Gibco) supplemented with 10% v/v fetal bovine serum (heat inactivated, cat. no. F4135, Merck), 5% (100 ug/ml) Penicillin/streptomycin, 50 ug/ml Geneticin

G418 (cat. no. 10131027, Gibco) and 0.25 ug/ml Puromycin (cat. no. 15490717, Thermo Fisher) at 37 °C with 5% CO2 in a humidified incubator.

Fluorescence Recovery After Photobleaching (FRAP)

We performed FRAP experiments to determine the diffusion rate of histidine-tagged proteins tethered to SLBs of different compositions. SLBs were formed in our PCR-tube based experimental chambers and labelled fluorescently by incubation with 10 nM His_6-GFP for 40 min followed by washing off unbound protein (replacement of 50 ul of the old buffer with fresh one for ten times). FRAP image sequences were recorded using a spinning disc confocal microscope (Ultraview Vox, Perkin Elmer) with a 100x objective (NA 1.40, oil, Plan Apo VC, Nikon) and equipped with a FRAP unit. The sample was illuminated, and the image window was adjusted to have uniform illumination. A region of interest of 5 µm diameter was drawn using ROI tool and saved for future use. Photobleaching was performed using the 488 nm laser at maximum power. Acquisition criteria was set to 10 frames before bleaching, and 4 mins of imaging after bleaching at a time interval of 5 s per frame. The same conditions were maintained for all samples. FRAP images were acquired with a Hamamatsu ORCA-R2 camera operated by Volocity 6.0 software (Perkin Elmer).

The mean intensity values of the FRAP region were bleach corrected using the readings of an area outside of the FRAP region and normalised by dividing the mean value from the pre-bleach image sequence. An exponential function was fitted to the recovery curve (T=0 is defined as the end of the bleach procedure), and the resulting time constant was used to calculate the diffusion constant using the equation describing fluorescence recovery of a circular region of radius w: $D = \frac{0.88\, w^2}{4\, \tau_{1/2}}$ (17).

Total Internal Reflection Fluorescence (TIRF) microscopy

TIRF microscopy is a method of choice to visualize fluorescently labelled objects in the vicinity of a surface while increasing the signal to noise ratio if the bulk phase also contains fluorescent species. TIRF microscopy was performed using a Nikon Eclipse Ti-E/B microscope equipped with perfect focus, a Ti-E TIRF illuminator (CW laser lines: 488 nm, 565 nm, 647 nm) and a Zyla sCMOS 4.2 camera (Andor, Oxford Instruments, UK) controlled by Andor iQ3 software. The TIRF mode was generated by illumination through the periphery of a high NA objective (100X, 1.45 NA).

Extended-Total Internal Reflection Fluorescence – Structured Illumination Microscopy

Super-resolution imaging was performed on a custom-built TIRF-SIM setup in the Fritzsche laboratory (Oxford university) based on a ferroelectric spatial light modulator used to generate diffraction patterns and adjust the TIRF angle (18, 19). The TIRF angle was selected to ensure below 150 nm penetration depth 488, 560, and 640 nm laser lines. Illumination and detection were performed through an Olympus 100× (NA 1.49; UPLAPO100XOHR) oil objective. Raw images were obtained on two Hamamatsu Orca Flash 4.0 cameras, and reconstructed with custom made software (18).

Image analysis

Cell area in TIRF images was calculated by measuring the area of actin staining utilising thresholding in FIJI. Curves were time-shifted to synchronise different fields, considering that cells were fully attached once they reach an area of 20 µm. Actin, E-cadherin and α-catenin recruitment show average intensity of signal in this area normalised to the highest average intensity reached in each cell. To calculate protrusion area, cell edges were first segmented using Otsu thresholding and a morphological opening with a 2.68µm filter was applied to generate a smoothened inner edge corresponding to the cell cortex. Protrusion area was then calculated as the area between the detected and smoothed edges.

Rate of photodamage is the rate of decrease in relative actin intensities in manually drawn ROIs containing different actin architectures, normalised to the intensity at the first time-point. Rate of growth of static bundles and rate of retrograde flow were measured from kymographs drawn along the direction of growth and flow respectively. PIV was carried out using PIVLAB in MATLAB. Each point on the graph represents average magnitudes of velocities at all points within a region of dynamic actin, further averaged over 30 time intervals. Areas of regions containing different actin architectures were estimated by manually drawing ROI in FIJI.

For statistical analysis, populations were first tested for normality using a Shapiro-Wilk test. Difference between means was tested using t-test with Welch's correction for populations conforming to normality and with Mann-Whitney test for population deviating from normality.

Figures

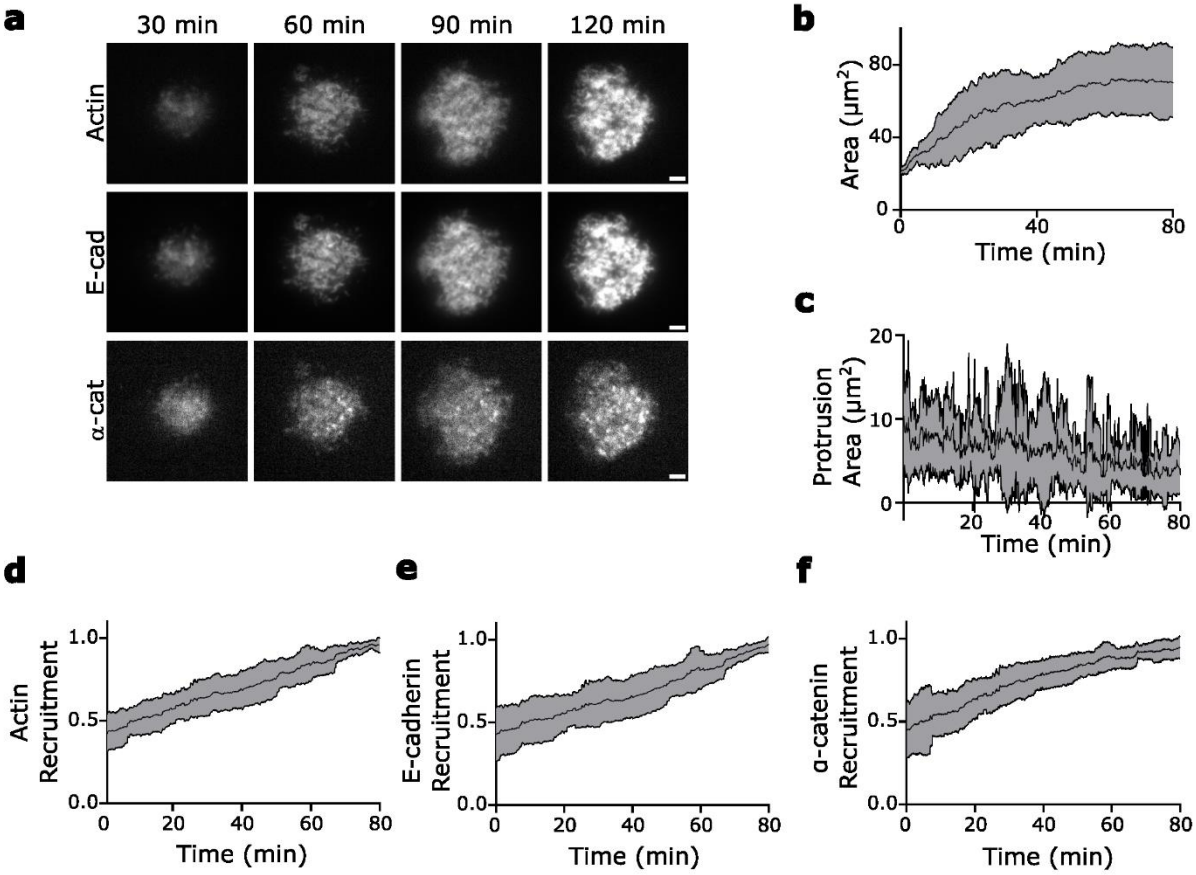

Fig 1: MCF7 cells form AJs on SLBs containing E-cadherinECD

a TIRF images of MCF7 cells expressing GFP-E-cadherin, LifeAct-mcherryTagRFPT and α-catenin-iRFP670 at indicated times post-seeding on SLBs containing E-cadherin extracellular domain. Scale Bar = 2μm. **b** Area of individual cells spreading over time. Mean ± SD plotted n=7. **c-e** Plots of relative intensity evolutions over time of LifeAct-TagRFPT, GFP-E-cadherin, and α-catenin-iRFP670; mean ± SD, n=14.

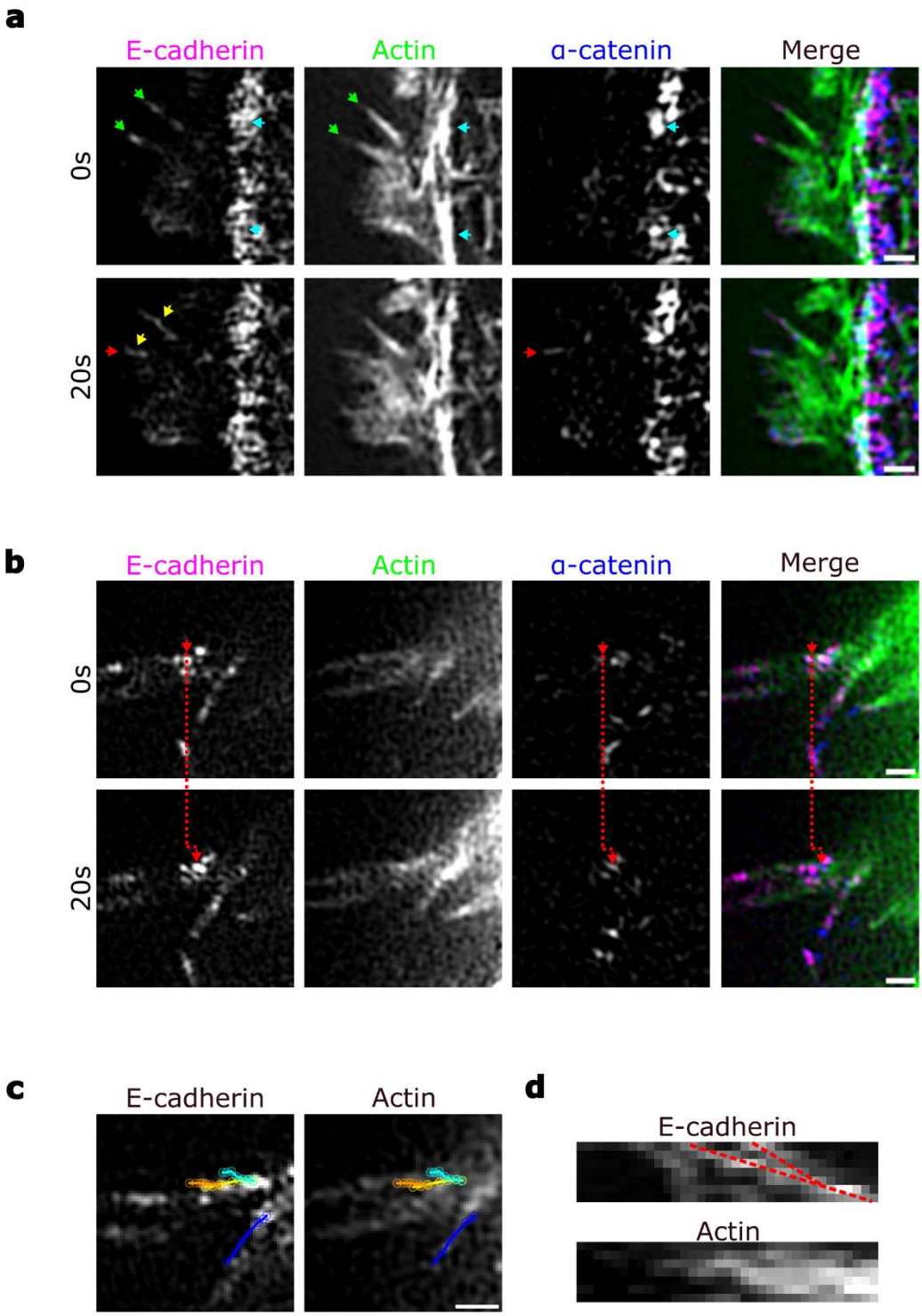

Fig. 2: AJs formed on SLBs are mobile structures.
a TIRF images of MCF7 cells expressing GFP-cadherin, LifeAct-TagRFPT, and α-catenin. Green arrows show E-cadherin recruited to the ends of actin filaments. Yellow arrows show lengthening of Cadherin staining along the filament. The red arrow shows α-catenin recruited to E-cadherin enriched structures. Cyan arrows show E-cadherin, α-catenin and actin colocalised in mature AJs. **b** E-cadherin and α-catenin puncta move over time **c** Tracks of the E-cadherin puncta moving along the actin filament. **d** Kymographs of E-cadherin and actin showing the movement and clustering of E-cadherin puncta. All scale bars are 0.5μm.

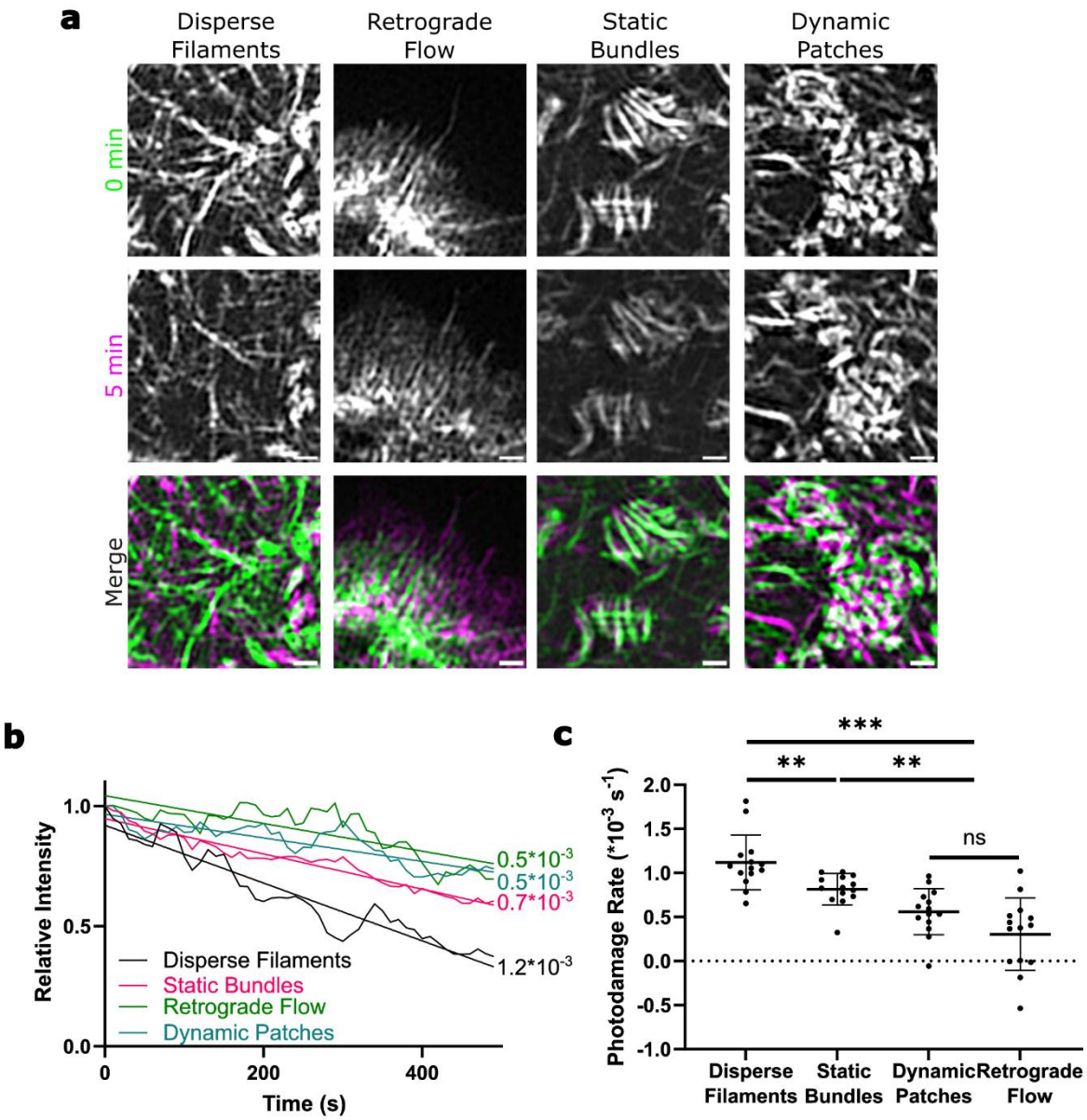

Fig 3: Types of actin architecture at AJs.

a TIRF-SIM images of 4 kinds of actin architecture in MCF7 cells before and after imaging of 5 mins at an interval of 10 s per image. Scale Bar = 0.5µm. **b** Representative curves of decrease in actin signal intensity over time in different actin architectures. **c** Rate of decrease in actin intensity in regions with different actin architectures. Mean ± SD plotted n=10 from N=2.

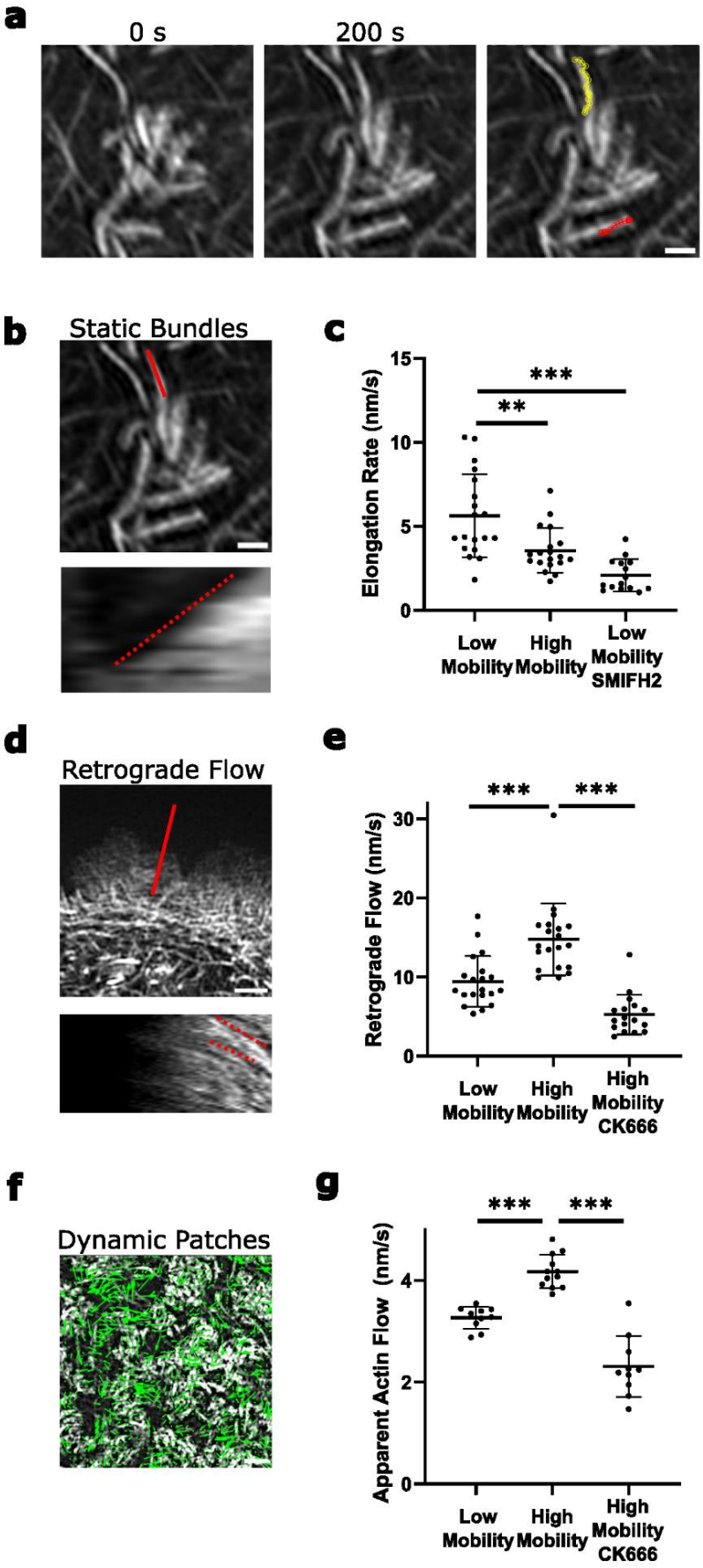
a
0 s
200 s
b
Static Bundles
c
Elongation Rate (nm/s)
15
10
5
0
***
**
Low Mobility
High Mobility
Low Mobility SMIFH2
d
Retrograde Flow
e
Retrograde Flow (nm/s)
30
20
10
0
***
***
Low Mobility
High Mobility
High Mobility CK666
f
Dynamic Patches
g
Apparent Actin Flow (nm/s)
4
2
0
***
***
Low Mobility
High Mobility
High Mobility CK666

Fig 4: The switch between branched and linear actin polymerisation depends on E-cadherin mobility.

a TIRF-SIM images static bundles of actin showing the extension of bundles (red and yellow lines show the track of the bundle tip over time) Scale Bar = 0.5μm **b** Kymographs along the red line give rate of actin bundle elongation. **c** Rates of actin bundle elongation in cells plated on low and high mobility substrates and in presence of formin inhibitor SMIFH2. Mean ± SD plotted from N=3 **d** Kymographs along the red line give rate of retrograde flow. Scale Bar = 1μm. **e** Rates of retrograde flow in cells plated on low and high mobility substrates and in presence of Arp2/3 inhibitor CK666. Mean ± SD plotted from N=3. **f** Velocity vectors from PIV analysis used to measure apparent actin flows in dynamic patches. Scale Bar = 1μm. **g** Apparent actin flows in dynamic patches in cells plated on low and high mobility substrates and in presence of Arp2/3 inhibitor CK666 Mean ± SD plotted from N=3.

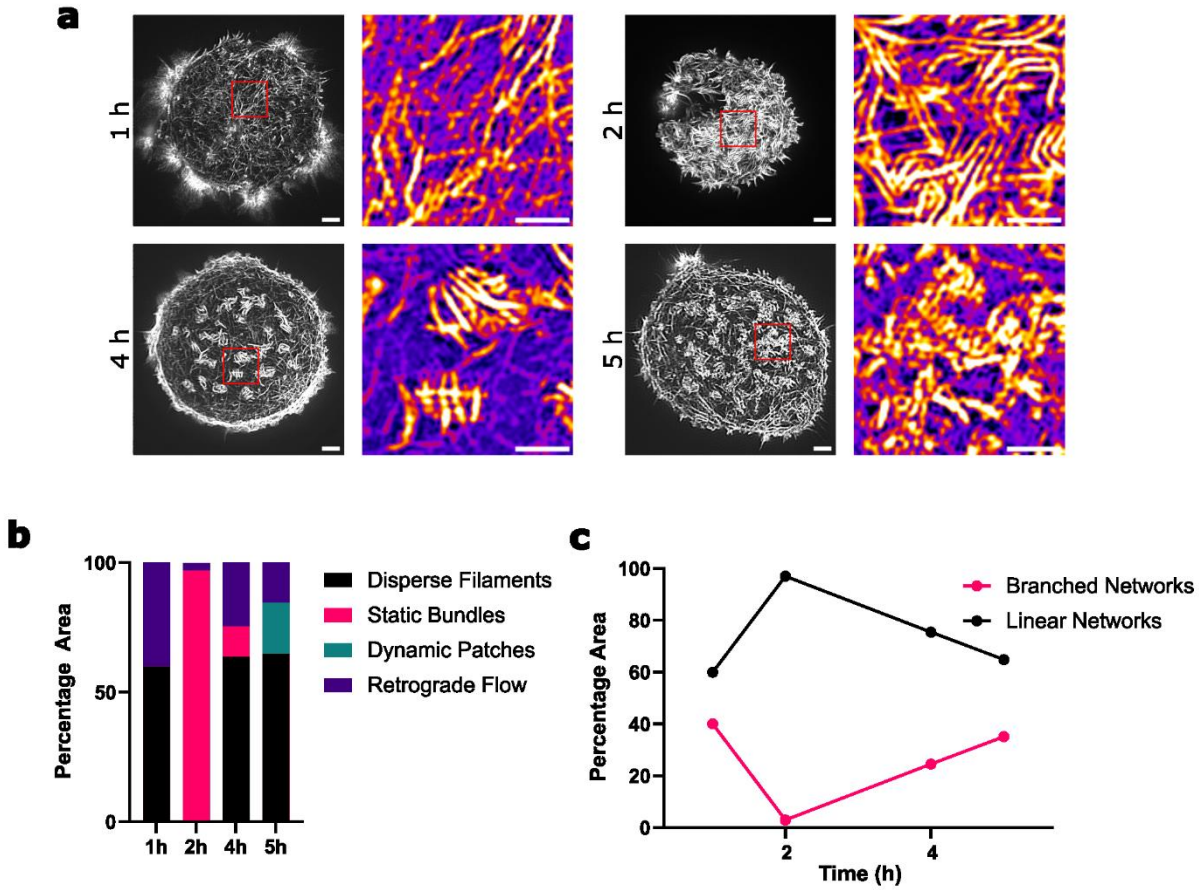

Fig. 5: Branched and linear polymerisation are temporally regulated during AJ maturation
a TIRF-SIM image of actin in MCF7 cells imaged at different times post-seeding. Scale Bar = 2μm. **b** Percentage of the cell covered by varying actin architectures at different times after seeding. **c** Percentage of the cell covered by branched and linear actin networks at different times after seeding. Data shown for one representative cell chosen from a set of N=3.

Supplement Figures

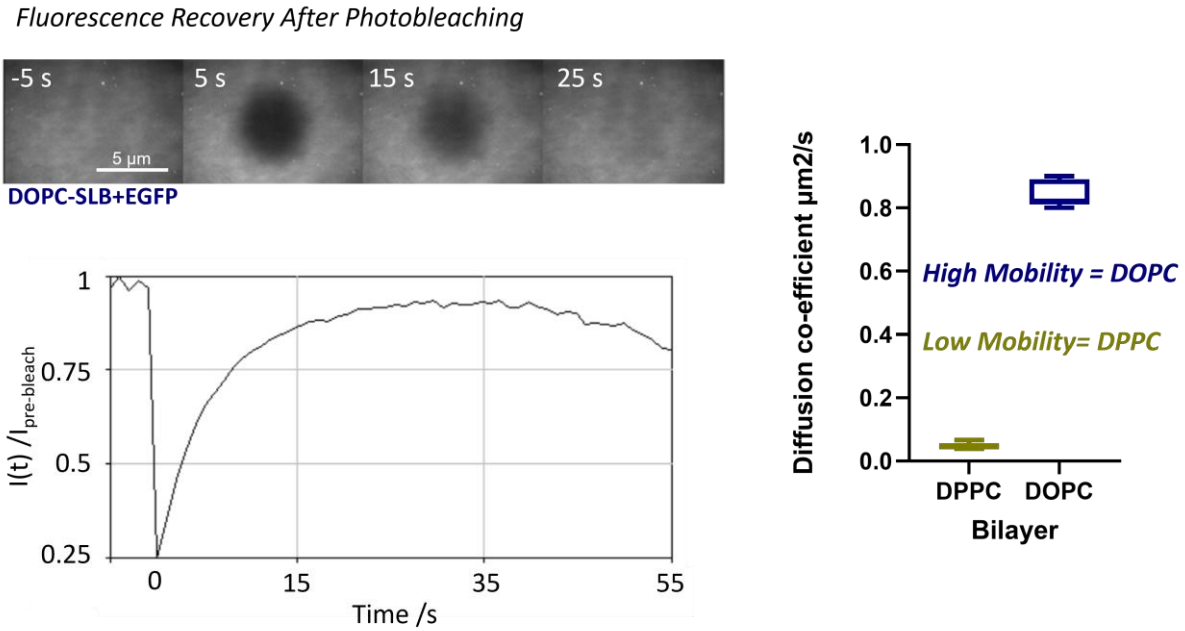

Sup. Fig. 5: Measurement of diffusion of proteins tethered to DOPC and DPPC lipid bilayers Example data-set and box plot summarising FRAP-based measurements of the diffusion coefficient of His6-GFP tethered to DOPC and DPPC SLBs; n ≥ 5 for each condition.

References

1. Charras G, Yap AS. Tensile Forces and Mechanotransduction at Cell–Cell Junctions. Current Biology. 2018;28(8):R445-R57.
2. Arslan FN, Eckert J, Schmidt T, Heisenberg CP. Holding it together: when cadherin meets cadherin. Biophysical Journal. 2021;120(19):4182-92.
3. Kobielak A, Pasolli HA, Fuchs E. Mammalian Formin-1 Participates in Adherens Junctions and Polymerization of Linear Actin Cables. Nature Cell Biology. 2004;6:21–30.
4. Acharya BR, K. WS, Lieu ZZ, Parton RG, Grill SW, Bershadsky AD, et al. Mammalian Diaphanous 1 Mediates a Pathway for E-Cadherin to Stabilize Epithelial Barriers through Junctional Contractility. Cell Reports. 2017;18(12):2854–67.
5. Grikscheit K, Frank T, Wang Y, Grosse R. Junctional Actin Assembly Is Mediated by Formin-like 2 Downstream of Rac1. The Journal of Cell Biology. 2015;209(3):367–76.
6. Lee NK, Fok KW, White A, Wilson NH, O'Leary CJ, Cox HL, et al. Neogenin Recruitment of the WAVE Regulatory Complex Maintains Adherens Junction Stability and Tension. Nature Communications. 2016;7:11082.
7. Michael M, Meiring JCM, Acharya BR, Matthews DR, Verma S, Han SP, et al. Coronin 1B Reorganizes the Architecture of F-Actin Networks for Contractility at Steady-State and Apoptotic Adherens Junctions. Developmental Cell. 2016;37(1):58-71.
8. Li J-XH, Tang VW, Boateng KA, Brieher WM. Cadherin Puncta Are Interdigitated Dynamic Actin Protrusions Necessary for Stable Cadherin Adhesion. Proceedings of the National Academy of Sciences of the United States of America. 2021;118(24).
9. Bertocchi C, Wang Y, Ravasio A, Hara Y, Wu Y, Sailov T, et al. Nanoscale architecture of cadherin-based cell adhesions. Nature Cell Biology. 2017;19(1):28-37.
10. Biswas KH, Hartman KL, Zaidel-Bar R, Groves JT. Sustained α-catenin Activation at E-cadherin Junctions in the Absence of Mechanical Force. Biophysical journal. 2016;111(5):1044-52.
11. Biswas KH, Hartman KL, Yu C-H, Harrison OJ, Song H, Smith AW, et al. E-cadherin junction formation involves an active kinetic nucleation process. Proceedings of the National Academy of Sciences of the United States of America. 2015;112(35):10932-7.
12. Arslan FN, Hannezo É, Merrin J, Loose M, Heisenberg C-P. Adhesion-induced cortical flows pattern E-cadherin-mediated cell contacts. Current Biology. 2024;34(1):171-82.e8.
13. Noordstra I, Hermoso MD, Schimmel L, Bonfim-Melo A, Currin-Ross D, Duong CN, et al. An E-cadherin-actin clutch translates the mechanical force of cortical flow for cell-cell contact to inhibit epithelial cell locomotion. Dev Cell. 2023;58(18):1748-63 e6.
14. Borghi N, Sorokina M, Shcherbakova OG, Weis WI, Pruitt BL, Nelson WJ, et al. E-cadherin is under constitutive actomyosin-generated tension that is increased at cell-cell contacts upon externally applied stretch. Proceedings of the National Academy of Sciences of the United States of America. 2012;109(31):12568-73.
15. Yamada S, Nelson WJ. Localized zones of Rho and Rac activities drive initiation and expansion of epithelial cell cell adhesion. The Journal of Cell Biology. 2007;178(3):517-27.
16. Köster DV, Bhat A, Talluri S, Mayor S. Reconstitution of Membrane-tethered Minimal Actin Cortices on Supported Lipid Bilayers. Journal of visualized experiments : JoVE. 2022;2022(185).
17. Axelrod D, Koppel DE, Schlessinger J, Elson E, Webb WW. Mobility measurement by analysis of fluorescence photobleaching recovery kinetics. Biophysical Journal. 1976;16(9):1055-69.
18. Li D, Shao L, Chen BC, Zhang X, Zhang M, Moses B, et al. Extended-resolution structured illumination imaging of endocytic and cytoskeletal dynamics. Science. 2015;349(6251):aab3500-aab.

19. Fritzsche M, Li D, Colin-York H, Chang VT, Moeendarbary E, Felce JH, et al. Self-organizing actin patterns shape membrane architecture but not cell mechanics. Nature Communications. 2017;8:14347-.